

A unified approach coupling linearized Navier-Stokes equations and Helmholtz equations to predict sound propagation with viscothermal losses in acoustic liners

Wei Na (那薇)^{1,2} Hua-Dong Yao (姚华栋)² Susann Boij^{1,3,4} Raimo Kabral⁵
Hans Bodén^{1,3} and Gunilla Efraimsson^{1,3,4}

¹*Department of Engineering Mechanics, KTH Royal Institute of Technology, Stockholm, Sweden*

²*Department of Mechanics and Maritime Sciences, Chalmers University of Technology, Gothenburg, Sweden*

³*The Marcus Wallenberg Laboratory for Sound and Vibration Research (MWL), Stockholm, Sweden*

⁴*The Centre for ECO2 Vehicle Design, Stockholm, Sweden*

⁵*Volvo Car Corporation, Gothenburg, Sweden*

(*Electronic mail: naweiflorence@gmail.com, now working at Volvo Group, Gothenburg, Sweden)

(Dated: 26 April 2023)

This paper introduces a unified approach for coupling the classical linearized Navier-Stokes equations (LNSE), the original Helmholtz equation and a modified form of the Helmholtz equation for porous material modelling in frequency domain. This approach is termed the unified LNSE (ULNSE). It accounts for viscothermal losses of sound propagation in acoustic liners with small-scale perforation. This method also provides a possibility to switch from LNSE to the classical and modified Helmholtz equations depending on local acoustic properties. The ULNSE is validated and applied to simulation of conventional and hybrid liners in three dimensions (3D), and also compared to a semi-empirical model and experiments. The hybrid acoustic liner consists of a perforated plate, a porous foam layer, and a rectangular cavity. Unlike the hybrid liner, the porous foam is not mounted in the conventional liners. In the perforated plate where the viscothermal effect plays a role, sound waves are solved using the LNSE. The modified Helmholtz equation is formulated with a complex wavenumber to model the porous foam as an equivalent fluid model. In the liner cavity and external duct, the original Helmholtz equation is utilized. The ULNSE is cheaper than the classical LNSE since the Helmholtz equations, which consume less computational resources, are used locally where the viscothermal losses are negligible. Meanwhile, the ULNSE can maintain high numerical accuracy. The liners are analyzed in terms of critical parameters such as the porous foam material, and perforated plate thickness and porosity. The porous foam proves to be effective in sound absorption.

I. INTRODUCTION

Noise emitted from turbomachines is one of the main contributors to environmental pollution caused by commercial aircraft¹ or future electric aircraft². This type of noise can be effectively reduced by installing acoustic liners in the walls of engine intakes and bypass ducts³. There is an increasing need for liners that are capable of absorbing noise over a wide range of frequencies, rather than just a few specific frequencies. In addition, liner technology has proven effective in reducing landing-gear noise through liners installed in landing-gear bay walls⁴.

The acoustic performance of a liner can be in general analyzed via semi-empirical models and experiments. However, semi-empirical models are less reliable to predict the acoustic performance, when the liner structure has a significant geometry change⁵, or when an extra layer of porous material is assembled within the liner. In an experimental test, the acoustic performance of a liner is in most cases initially measured with an impedance duct, for example, the previous studies in Zhou and Bodén⁶ and Kabral, Du, and Åbom⁷. However, in the early stage design of liners, rapid numerical methods with high accuracy are more useful for the purpose of technical iterations.

Due to the recent blooming of Computational Aeroacoustics (CAA), there have been a wide body of researches on numerical methodologies for liner acoustics^{8–12}. For example, Zhang and Bodony¹³ studied the interaction between grazing laminar flow and turbulent boundary layer in a cavity-backed circular orifice using Direct Numerical Simulation (DNS). Sovardi, Jaensch, and Polifke¹⁴ analyzed the aeroacoustic scattering and noise sources in a duct with an orifice using Large Eddy Simulation (LES). However, DNS and LES, as well as other advanced high-fidelity CFD methods, are often computationally demanding¹⁵. It is of interest to develop a reduced-order numerical approach, which is less expensive.

Linearized Navier-Stokes Equations (LNSE) have been proposed in terms of the physical characteristics of flow and sound waves, e.g. by Aurégan, Starobinski, and Pagneux¹⁶, to reduce computational cost but provide an accurate acoustic prediction. The LNSE can resolve viscothermal losses in acoustic boundary layers, which have a strong damping effect on sound waves. The viscothermal losses usually exist inside small geometrical structures such as holes of perforated or micro-perforated plates. As acoustic liners feature in small openings, the losses have been taken into account in the relevant assessment^{17–19}.

Vandemaele *et al.*²⁰ used the LNSE in time domain to simulate sub-millimeter orifices in a

quiescent medium and in the presence of grazing flow. On the other hand, the LNSE in the frequency domain have also been put forward^{21–24}. Weng, Boij, and Hanifi²⁵ studied turbulence at Mach numbers in pipes with rigid walls. By developing an eddy-viscosity model for the LNSE in the frequency domain, an eigenvalue approach was proposed to identify the wavenumbers of axisymmetric plane waves inside the pipes. Sack, Abom, and Efraimsson²⁶ developed a multi-port eigenvalue method to analyze high-order modes of flow in ducts with the viscous-thermal damping. Temiz *et al.*⁹ established an incompressible LNSE method to investigate end-correction coefficients for flow in a duct with an orifice.

As sound waves propagate within ducts or cavities such as Helmholtz resonators, the propagation is usually regarded to be isentropic because of negligible viscothermal effects. The case can be directly simulated using the wave propagation equation with or without flow convection, or the Helmholtz equation in the frequency domain. The LNSE's advantage to capture the viscothermal effects is not needed for the linear propagation. And the LNSE accounts for more computational costs than the wave propagation equation and Helmholtz equation.

However, acoustic liners comprise distinct parts: Helmholtz resonator cavities and perforated plates. A conventional liner commonly contains a perforated plate between rectangular cavities that are Helmholtz resonators. In contrast, a perforated plate in a hybrid liner is added with a porous metallic foam to increase acoustic absorption. The viscous effects are only significant near the perforated plates. It is less efficient to use the LNSE to simulate all the parts including the Helmholtz resonators. Therefore, the current study is motivated to develop a unified LNSE (ULNSE) approach that couples the classical LNSE and Helmholtz equations and sets them to different regions in a computational domain in terms of the significance of the viscothermal damping effects. Based on the previous studies^{21–24}, the present ULNSE approach will be developed to be applicable for 3D cases. It is worth noting that the approach will be validated based on liners within quiescent mediums in the current study. When a flow is present, the convection effect can be accounted for by including an additional convection term in the governing equations of the present approach, as in previous studies²⁰. Nevertheless, it is interesting to extend the present approach to include this feature in the future.

The paper is organized as follows: In Section II, the ULNSE approach is presented. The algorithms for coupling the LNSE and Helmholtz equations in the unified approach are validated in terms of the continuity of acoustic perturbations at the interface between the two equation systems in Section III. A typical hybrid liner is described in Section IV A, followed by the description of

the numerical model established based on the ULNSE approach in Section IV B. The results of a conventional liner, in which a perforated plate is designed with different parameters, are analyzed in Section V. And the ULNSE approach is compared to a semi-empirical model and experiments. Afterwards, the new approach is applied to simulating a hybrid liner with a porous metallic foam in Section IV D. The conclusions are summarized in Section VII.

II. GOVERNING EQUATIONS OF ULNSE

In this section, the governing equations of the ULNSE approach are presented. We first present the three-dimensional LNSE in the frequency domain, including the energy equation. Thereafter, an equivalent fluid model is introduced to model sound propagation in a porous material. Then, the algorithms for coupling the LNSE and the Helmholtz equations are described. The post-processing method for results is a two-microphone method (TMM).

The ULNSE approach proposed in this study has the advantage of computing viscothermal losses and sound propagation simultaneously. In the practice of the ULNSE, the classical LNSE is used in regions where the sound attenuation caused by the viscothermal effects is significant, and the Helmholtz equation in the rest of the computational domain. The coupling of these equations consumes less computational resources but retains numerical accuracy compared to the classical LNSE.

A. Classical LNSE in frequency domain

A modeling framework of LNSE in either the 2D Cartesian coordinates or axisymmetric cylindrical coordinates was proposed by Kierkegaard, Boij, and Efraimsson²¹ and Kierkegaard *et al.*²². After that, the modeling framework was extended to 3D in the Cartesian coordinates by Kierkegaard, Efraimsson, and Agarwal²⁷ and Na, Efraimsson, and S.Boij²⁸. However, these previous studies adopted an isentropic assumption to relate acoustic pressure perturbations to acoustic density perturbations. By doing this, the acoustic energy equation was decoupled in the previous methods. In contrast, the ULNSE includes both viscous losses (due to acoustic velocity gradient) and thermal losses (due to temperature gradient).

The classical LNSE is derived based on the compressible Navier-Stokes equations. The fluid is

assumed to be a perfect gas, yielding

$$e = c_v T, \quad p = R\rho T, \quad c_p = c_v + R, \quad (1)$$

where e is the internal energy per unit mass, and c_v and c_p are the heat capacities of constant volume and constant pressure, respectively. The coefficient R is the specific gas constant.

The governing equations of the compressible Navier-Stokes equations regardless of body forces read:

$$\frac{D\rho}{Dt} + \rho \frac{\partial u_i}{\partial x_i} = 0, \quad (2)$$

$$\rho \frac{Du_i}{Dt} = -\frac{\partial p}{\partial x_i} + \mu_B \frac{\partial^2 u_j}{\partial x_i \partial x_j} + \frac{\partial \tau_{ij}}{\partial x_j}, \quad (3)$$

$$c_p \rho \frac{DT}{Dt} - \frac{Dp}{Dt} = \frac{\partial}{\partial x_i} \left(\kappa_{th} \frac{\partial T}{\partial x_i} \right) + \phi(\mu, \mu_B, u_i), \quad (4)$$

where ρ denotes the density, u_i ($i = 1, 2, 3$) is the component of the velocity vector, p is the pressure. The coefficient μ_B is the bulk viscosity that accounts for the rotational and translational modes of molecular motions in mutual thermodynamic equilibrium, and μ denotes the dynamic viscosity²⁹. The viscous stress tensor is $\tau_{ij} = \mu (\partial u_i / \partial x_j + \partial u_j / \partial x_i - 2\partial u_k / \partial x_k \delta_{ij})$. In the last equation, T represents the temperature, and κ_{th} the thermal conductivity. Due to the shear viscosity and fluid relaxation losses, the viscous dissipation of mechanical energy, ϕ , is defined as

$$\phi(\mu, \mu_B, u_i) = \mu \left(\frac{\partial u_i}{\partial x_j} \frac{\partial u_i}{\partial x_j} + \frac{\partial u_j}{\partial x_i} \frac{\partial u_i}{\partial x_j} \right) - \left(\frac{2}{3}\mu - \mu_B \right) \left(\frac{\partial u_i}{\partial x_i} \right)^2. \quad (5)$$

To describe acoustic attenuation or absorption, the terms associated with the bulk viscosity μ_B must be considered in the momentum equations. The reason is that the mean pressure in a deforming viscous fluid is different from the thermodynamic pressure²⁹⁻³¹. Moreover, the energy equation is required to describe viscothermal effects, for example, heat conduction or energy losses in a acoustic boundary layer^{32,33}.

The first step in the linearization of the compressible Navier-Stokes equations is to decompose every physical quantity into mean and perturbed parts. Take the density for example, $\rho = \bar{\rho} + \rho'$, where the over-bar denotes the average operation, and the prime denotes the perturbation. The perturbed part is assumed to be harmonic time-dependent. For the density, the perturbed part is written to $\rho'(x, t) = \text{Re}\{\hat{\rho}(x)e^{i\omega t}\}$. Here the hat $\hat{\cdot}$ denotes the variable in the frequency domain, and ω is the angular frequency³⁴.

Considering sound wave propagation in a quiescent medium (i.e., the mean velocity $\bar{u}_i = 0$), the LNSE is written as

$$i\omega\hat{p} + \frac{\partial\bar{\rho}\hat{u}_i}{\partial x_i} = 0, \quad (6)$$

$$i\omega\bar{\rho}\hat{u}_i = -\frac{\partial\hat{p}}{\partial x_i} + \mu\left(\frac{\partial^2\hat{u}_i}{\partial x_j\partial x_j} + \frac{1}{3}\frac{\partial^2\hat{u}_j}{\partial x_i\partial x_j}\right) + \mu_B\frac{\partial^2\hat{u}_j}{\partial x_i\partial x_j}, \quad (7)$$

$$i\omega\bar{\rho}c_p\hat{T} + c_p\bar{\rho}\hat{u}_i\frac{\partial\bar{T}}{\partial x_i} - i\omega\hat{p} - \hat{u}_i\frac{\partial\bar{p}}{\partial x_i} = \frac{\partial}{\partial x_i}\left(\kappa_{th}\frac{\partial\hat{T}}{\partial x_i}\right). \quad (8)$$

To close the equation system, an additional relationship based on the linearized ideal gas law is introduced:

$$\frac{\hat{p}}{\bar{p}} = \frac{\hat{\rho}}{\bar{\rho}} + \frac{\hat{T}}{\bar{T}}. \quad (9)$$

B. Modified Helmholtz equation and equivalent fluid model for porous material

The sound propagation in a porous material can be modeled with an equivalent fluid model. The porous material is treated to be equivalent to a “fluid” with damping. To take into account the damping effect, complex wavenumbers are introduced to replace real wavenumbers in the Helmholtz equation. It yields the modified Helmholtz equation:

$$\frac{\partial^2\hat{p}}{\partial x_i\partial x_i} + k_{eq}^2\hat{p} = 0, \quad (10)$$

where k_{eq} is the complex wavenumber.

The complex wavenumber can be modeled in various ways. One of the ways is the Delany-Bazley model, while the use of the model is limited due to a number of restrictions³⁵. The model was then improved by Miki³⁶ as

$$k_{eq} = \frac{\omega}{c_0}(1 + 7.81X^{-0.618} - i \cdot 11.41X^{-0.618}), \quad (11)$$

where ω represents the angular frequency, and c_0 denotes the speed of sound. The dimensionless parameter X is defined as

$$X = \rho_0 f / \sigma, \quad (12)$$

where f represents the frequency, ρ_0 is the density, and σ is the resistivity of the porous material. The subscript '0' indicates that the density and speed of sound are counted in the freestream flow rather than in the porous material. This model is empirically based. It is valid for $0.01 < X < 1.0$, corresponding to $1000 < \sigma < 50000 \text{ Pa} \cdot \text{s} \cdot \text{m}^{-2}$.

C. Coupling algorithms

To couple the LNSE with the modified Helmholtz equation, algorithms are developed for the acoustic pressure, acoustic particle velocity and acoustic temperature at an interfaces between different regions where either the LNSE or the modified Helmholtz equation is applied to.

The viscous term is neglected at the interface. Thus, the momentum equation in frequency domain, Eq. (7), is reduced to $i\omega\bar{\rho}\hat{u}_i = \partial\hat{p}/\partial x_i$. This relates the acoustic particle velocity to the acoustic pressure. As a result, the coupling algorithm for fulfilling the continuity of the acoustic particle velocity at the interface is written as:

$$\hat{u}_i^L n_i^L = \frac{1}{i\omega\bar{\rho}} \frac{\partial\hat{p}^H}{\partial x_i} n_i^H, \quad (13)$$

where n_i^L is the interface-normal vector pointing outwards from the side imposed with the LNSE, and n_i^H is the interface-normal vector points outwards from the other side imposed with the classical Helmholtz equation.

By substituting Eq. (13) into the left-hand side of Eq. (7), the coupling algorithm for satisfying the continuity of the acoustic pressure at the interface is obtained:

$$\left[-\hat{p}^L \delta_{ij} + \mu \left(\frac{\partial\hat{u}_i^L}{\partial x_j} + \frac{\partial\hat{u}_j^L}{\partial x_i} \right) - \left(\frac{2}{3}\mu - \mu_B \right) \left(\frac{\partial\hat{u}_k^L}{\partial x_k} \right) \delta_{ij} \right] n_j^L = \hat{p}^H n_i^H. \quad (14)$$

Based on the assumption that no heat transfers across the interface, the coupling algorithm for the continuity of the temperature is derived:

$$\kappa_{\text{th}} \frac{\partial\hat{T}^L}{\partial x_i} n_i^L = 0. \quad (15)$$

D. Finite element method for ULNSE

The LNSE of Eqs. (6) – (8) are discretized using a standard Galerkin finite element method (FEM)^{8,37}. A weak-form solution with weighted residuals for the governing equations is adopted in the FEM. The procedure of the discretization is explained as follows.

Based on the governing equations, variable residuals are multiplied with weighting functions. Integration in space is then performed for the residual equations, leading to the weak-form solution. The solution function space is defined as $S_{\hat{p},\hat{u}_i,\hat{T}}$. The variables in the weak-form equations are \hat{p} , \hat{u}_i , and \hat{T} . The weighting function space is defined as $\Psi_{\hat{p},\hat{u}_i,\hat{T}}$ with the variables in the

weighting function such as $w_{\hat{\rho}}$, $w_{\hat{u}_i}$, and $w_{\hat{T}}$. The weak-form governing equations are written as:

$$(w_{\hat{\rho}}, \mathbf{i}\omega\hat{\rho})_{\Omega} + \left(w_{\hat{\rho}}, \frac{\partial \bar{\rho} \hat{u}_i}{\partial x_i} \right)_{\Omega} = 0, \quad \forall w_{\hat{\rho}} \in \Psi_{\hat{\rho}}, \quad (16)$$

$$\begin{aligned} & (w_{\hat{u}_i}, \mathbf{i}\omega\bar{\rho}\hat{u}_i)_{\Omega} + \left(\frac{\partial w_{\hat{u}_i}}{\partial x_i}, \hat{p} \right)_{\Omega} \\ & - \left(w_{\hat{u}_i}, \boldsymbol{\mu} \left(\frac{\partial^2 \hat{u}_i}{\partial x_j \partial x_j} + \frac{1}{3} \frac{\partial^2 \hat{u}_j}{\partial x_i \partial x_j} \right) \right)_{\Omega} \\ & - \left(w_{\hat{u}_i}, \boldsymbol{\mu}_B \frac{\partial^2 \hat{u}_j}{\partial x_i \partial x_j} \right)_{\Omega} + (w_{\hat{u}_i}, h_{u_i})_{\partial\Omega_N} = 0, \quad \forall w_{\hat{u}_i} \in \Psi_{\hat{u}_i}, \end{aligned} \quad (17)$$

$$\begin{aligned} & (w_{\hat{T}}, \mathbf{i}\omega\bar{\rho}c_p\hat{T})_{\Omega} + \left(w_{\hat{T}}, c_p\bar{\rho}\hat{u}_i \frac{\partial \bar{T}}{\partial x_i} \right)_{\Omega} \\ & - (w_{\hat{T}}, \mathbf{i}\omega\hat{p})_{\Omega} - \left(w_{\hat{T}}, \hat{u}_i \frac{\partial \bar{p}}{\partial x_i} \right)_{\Omega} \\ & - \left(w_{\hat{T}}, \frac{\partial}{\partial x_i} \left(\boldsymbol{\kappa}_{th} \frac{\partial \hat{T}}{\partial x_i} \right) \right)_{\Omega} = 0, \quad \forall w_{\hat{T}} \in \Psi_{\hat{T}}, \end{aligned} \quad (18)$$

where $(\cdot, \cdot)_{\Omega}$ and $(\cdot, \cdot)_{\partial\Omega_N}$ mean the L_2 -inner product in the domain Ω and on the Neumann boundary $\partial\Omega_N$, respectively.

For the momentum equation, a neutral condition is imposed on the Neumann boundary, reading³⁸:

$$(-\hat{p}\delta_{ij} + \tau_{ij}(\hat{u}_k))n_j = h_{\hat{u}_i} \quad \text{on} \quad \partial\Omega_N. \quad (19)$$

The computational domain is discretized into finite elements to derive the weak-form solution. The variables in the solution is discrete, denoted with the superscript h . The approximations of the discrete variables are formulated with polynomial functions to yield

$$\hat{\rho}^h = \sum_{A=1}^{N_{dofs}} N_A \hat{\rho}_A, \quad \hat{u}_i^h = \sum_{A=1}^{N_{dofs}} N_A \hat{u}_{iA}, \quad \hat{T}^h = \sum_{A=1}^{N_{dofs}} N_A \hat{T}_A, \quad (20)$$

where $\hat{\rho}_A$, \hat{u}_{iA} and \hat{T}_A are the unknowns, and N_A is the shape function defined for the variable approximation. which are mostly represented by polynomial functions. The number of degrees of freedom (DOF) is denoted by N_{dofs} .

The approximations of the weighting functions are written as

$$w_{\hat{\rho}}^h = \sum_{B=1}^{N_{dofs}} N_B w_{\hat{\rho},B}, \quad w_{\hat{u}_i}^h = \sum_{B=1}^{N_{dofs}} N_B w_{\hat{u}_i,B}, \quad w_{\hat{T}}^h = \sum_{B=1}^{N_{dofs}} N_B w_{\hat{T},B}. \quad (21)$$

where N_B is the shape function specified for the weighting function.

The Lagrangian shape functions are adopted in Eqs. (20) and (21) in this study. Then, the standard Galerkin finite element equations in the discrete form are derived as follows.

$$B(w_{\hat{\rho}}^h, \hat{\rho}^h)_{\Omega} = (w_{\hat{\rho}}^h, i\omega \hat{\rho}^h)_{\Omega} + \left(w_{\hat{\rho}}^h, \frac{\partial \bar{\rho} \hat{u}_i^h}{\partial x_i} \right)_{\Omega}, \quad (22)$$

$$\begin{aligned} B(w_{\hat{u}}^h, \hat{u}^h)_{\Omega} = & (w_{\hat{u}}^h, i\omega \bar{\rho} \hat{u}_i^h)_{\Omega} + \left(\frac{\partial w_{\hat{u}}^h}{\partial x_i}, \hat{p}^h \right)_{\Omega} \\ & - \left(w_{\hat{u}}^h, \mu \left(\frac{\partial^2 \hat{u}_i^h}{\partial x_j \partial x_j} + \frac{1}{3} \frac{\partial^2 \hat{u}_j^h}{\partial x_i \partial x_j} \right) \right)_{\Omega} \\ & - \left(w_{\hat{u}}^h, \mu_B \frac{\partial^2 \hat{u}_j^h}{\partial x_i \partial x_j} \right)_{\Omega}, \end{aligned} \quad (23)$$

$$\begin{aligned} B(w_{\hat{T}}^h, \hat{T}^h)_{\Omega} = & (w_{\hat{T}}^h, i\omega \bar{\rho} c_p \hat{T}^h)_{\Omega} + \left(w_{\hat{T}}^h, c_p \bar{\rho} \hat{u}_i^h \frac{\partial \bar{T}^h}{\partial x_i} \right)_{\Omega} \\ & - \left(w_{\hat{T}}^h, i\omega \hat{p}^h \right)_{\Omega} - \left(w_{\hat{T}}^h, \hat{u}_i^h \frac{\partial \bar{p}}{\partial x_i} \right)_{\Omega} \\ & - \left(w_{\hat{T}}^h, \frac{\partial}{\partial x_i} \left(\kappa_{th} \frac{\partial \hat{T}}{\partial x_i} \right) \right)_{\Omega}. \end{aligned} \quad (24)$$

Simulations are carried out in COMSOL 5.0, which is a commercial finite element method (FEM) solver.

E. Post-processing with two-microphone method

The two-microphone method (TMM) has been put forward to compute the acoustic impedance and reflection coefficient^{39–41}. In this study, the TMM is employed to identify the acoustic characteristics of liners in an impedance duct.

In an impedance duct that has rigid walls, sound waves below the first cut-off frequency are plane waves. Therefore, the acoustic pressure of the sound waves in the frequency domain is formulated to

$$\hat{p}(x, f) = \hat{p}_+(f) \exp(-ikx) + \hat{p}_-(f) \exp(ikx), \quad (25)$$

where the symbol \pm means the positive and negative wave propagation direction along the x -axis.

According to Eq. (25), the incident wave at a specific wavenumber in the straight duct accounts for \hat{p}_+ , and the reflected wave for \hat{p}_- . To capture the acoustic pressure of the waves, two microphones are positioned using the TMM. The setup in both numerical simulations and experiments is shown in Fig. 1.

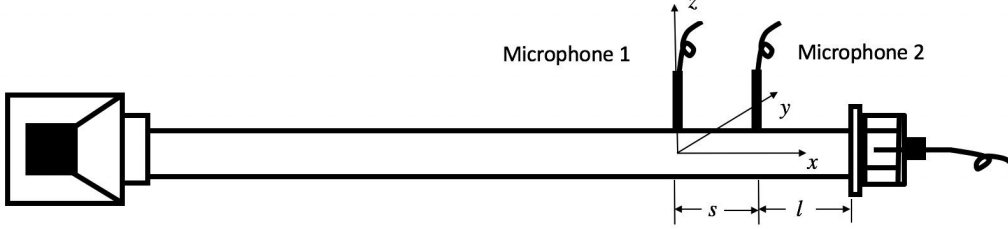


FIG. 1. Schematic of the TMM setup in the straight impedance duct, which is set in both numerical simulations and experiments. Here the distance between the microphones is $s = 0.01$ m, and the distance between Microphone 2 and the sound wave actuator is $l = 0.06$ m. The acoustic absorption cavity is positioned at the duct end on the left side.

The total acoustic pressure at the two microphones, \hat{p}_1 and \hat{p}_2 , are expressed as

$$\hat{p}_1 = \hat{p}_+(f) + \hat{p}_-(f), \quad (26)$$

$$\hat{p}_2 = \hat{p}_+(f)\exp(-iks) + \hat{p}_-(f)\exp(iks), \quad (27)$$

where s is the distance between the microphones (see Fig. 1).

By manipulating the equations of the total pressure, it yields the pressure components \hat{p}_+ and \hat{p}_- :

$$\hat{p}_+(f) = \frac{\hat{p}_1(f)\exp(iks) - \hat{p}_2(f)}{\exp(iks) - \exp(-iks)}, \quad (28)$$

$$\hat{p}_-(f) = \frac{-\hat{p}_1(f)\exp(-iks) + \hat{p}_2(f)}{\exp(iks) - \exp(-iks)}. \quad (29)$$

The reflection coefficient is defined to be:

$$R(f) = \hat{p}_-(f)/\hat{p}_+(f), \quad (30)$$

This coefficient should satisfy the physical condition of $|R| \leq 1$. In other words, the reflected wave pressure cannot exceed that of the incident wave.

The normalized impedance is derived on the basis of the reflection coefficient:

$$Z(f) = \frac{1 + R(f)}{1 - R(f)}. \quad (31)$$

III. VALIDATION OF COUPLING ALGORITHMS

In this section, the coupling algorithms are validated based on a benchmark case that a sound wave propagates across two regions that are solved with the LNSE and the Helmholtz equations.

Figure 2 illustrates the benchmark case. A plane sound wave propagates in a straight rectangular duct with a constant cross sectional area. The computational domain in the duct is divided into four segments. The acoustic methods are applied to the segment in the order from upstream to downstream as: the Helmholtz equation, the LNSE, the equivalent fluid model based on the modified Helmholtz equation, and the Helmholtz equation. The source of the plane wave is positioned at the upstream boundary of the computational domain.

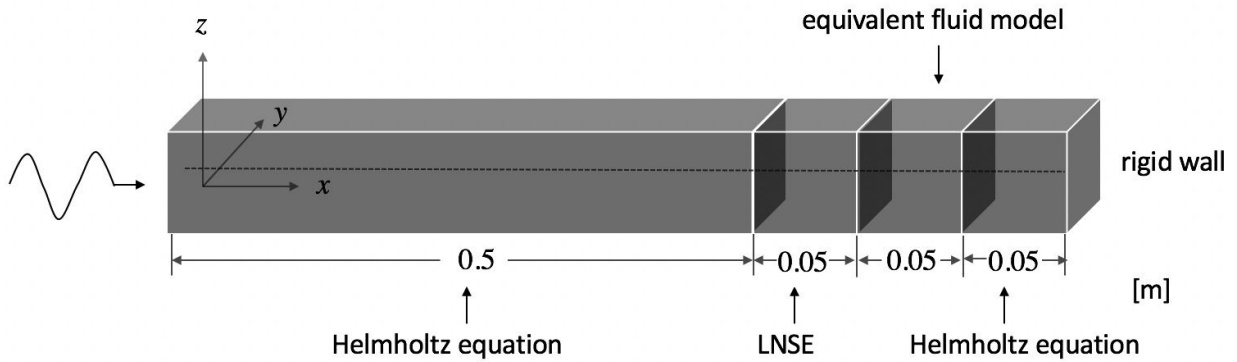


FIG. 2. Schematic of the benchmark case set to validate the coupling algorithms of the ULNSE. The dash line indicates the duct central line. The lengths of the segments are scale for the easy of illustration.

To verify the continuity of the acoustic pressure, its amplitudes and gradients are monitored along the central line of the duct. See the position of the center line in Fig. 2. The segment in $X \in (0.5, 0.55)$ is solved using the LNSE, and the remaining three segments using the original and modified Helmholtz equations. An equivalent fluid model is established in the modified Helmholtz equations.

The numerical results computed using the ULNSE approach are plotted in Fig. 3. As can be seen, the acoustic pressure amplitudes are continuous across the four segments of the duct, which are simulated with the different acoustic methods. The same continuous phenomenon is also observed for the acoustic pressure gradients. This demonstrates the continuity of the acoustic pressure obtained from the ULNSE, since there would be sudden pressure jumps at the interfaces between the segments if the discontinuity exists. In other words, the coupling algorithms of the ULNSE approach in Eqs. (13), (14) and (15) introduce negligible numerical reflection and losses

at the segment interfaces.

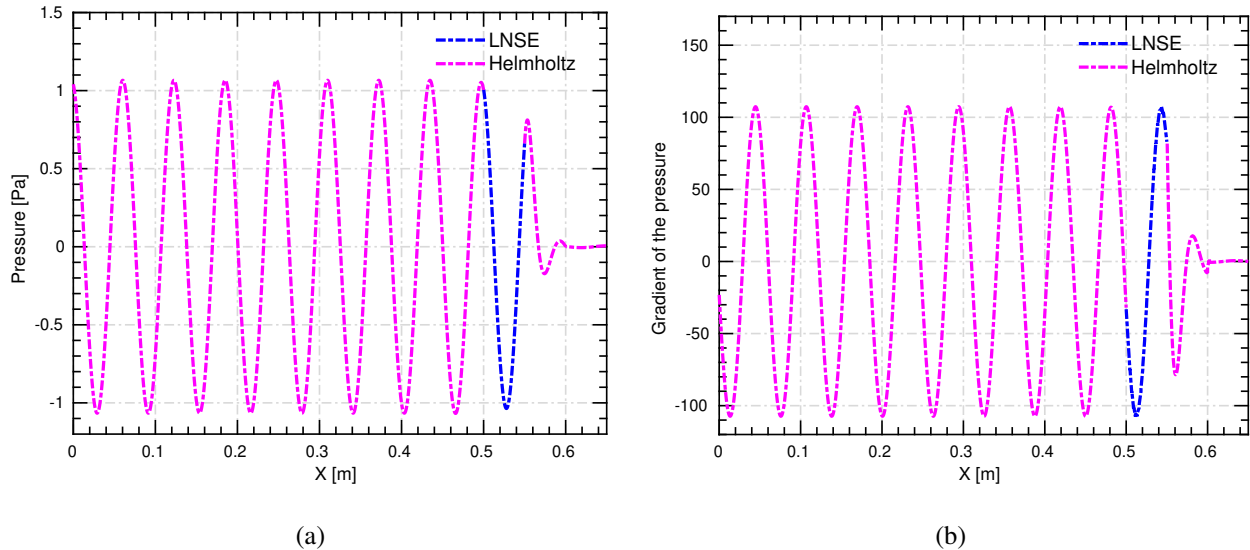


FIG. 3. (a) The amplitudes and (b) gradients of the acoustic pressure along the central line of the duct in the x-axis direction, which are computed for the benchmark case to validate the ULNSE approach. The segment solved with the LNSE is highlighted in blue, and the other segments with the (original and modified) Helmholtz equations in magenta.

IV. APPLICATION OF ULNSE TO HYBRID LINER

A. Description of hybrid liner

The hybrid liner investigated in this paper is shown in Fig. 4. A single cell of the liner comprises a perforated plate, porous metallic foam and Helmholtz cavity. The liner has also been tested in experiments regarding different component parameters. A test sample contains 32 cells. In the numerical simulations performed in this paper, we assume that aerodynamic or acoustic interactions between the cells of a liner are negligible. Besides, the vibration of the liner structure is excluded from the simulations although the vibration were noticed in the experiments. Based on these assumptions, the numerical models in the simulations are established for only single cells with different parameters, to save computational resources.

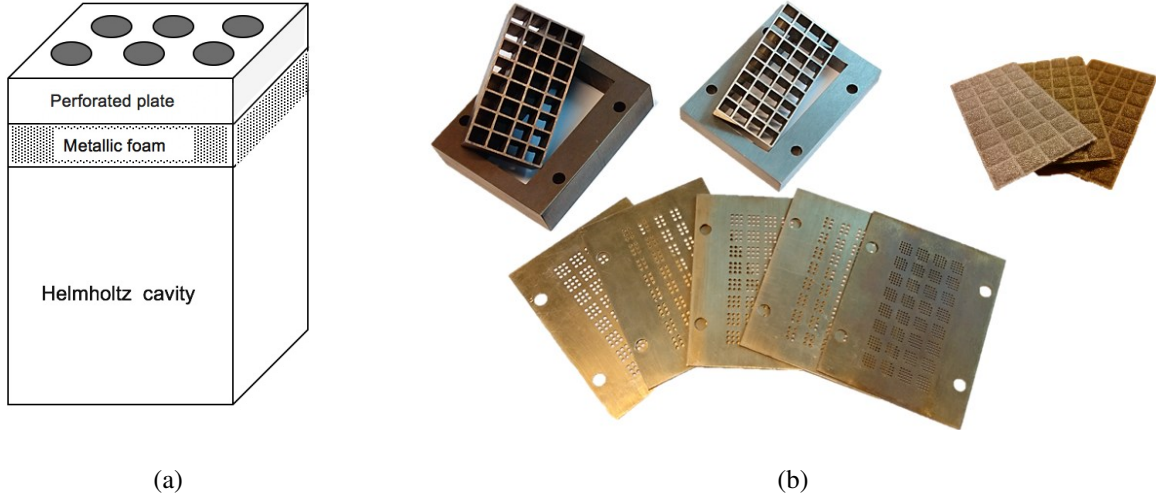


FIG. 4. (a) Schematic of a single cell of the hybrid liner. (b) The components of the test sample of the liner with 32 cells: the cavities (top left and middle), the porous metallic foams (top right), the perforated plates (bottom).

B. Numerical setup

The computational domain and numerical settings are schematized in Fig. 5. A rectangular duct is installed with a single hybrid liner cell at the end of the duct. The computational domain is split into four segments, each of which is simulated with an acoustic method constituting the ULNSE. The thickness of the perforated plate is $t_p = 1.2$ mm. The thickness of the metallic foam (i.e., the porous material) is $t_f = 1$ mm. The flow resistivity of the metallic foam is $[\sigma] = 34\,300 \text{ Pa} \cdot \text{s} \cdot \text{m}^{-2}$. The original Helmholtz equation is applied to the domain segments of the duct and liner cavity. The equivalent fluid model for the porous medium based on the modified Helmholtz equation is used in the segment where the porous metallic foam is located. The LNSE is used in the circular passages in the perforated plate, to resolve the acoustic boundary layers bringing about the viscothermal losses. The coupling algorithms are applied to the interfaces between the domain segments.

For the walls of the domain segments simulated with the original and modified Helmholtz equations (i.e., the duct, porous metallic foam and liner cavity), the boundary condition is set to the acoustic hard wall:

$$\frac{\partial \hat{p}}{\partial n} = 0. \quad (32)$$

The walls of the domain segment simulated with the LNSE (i.e., the circular passages formed

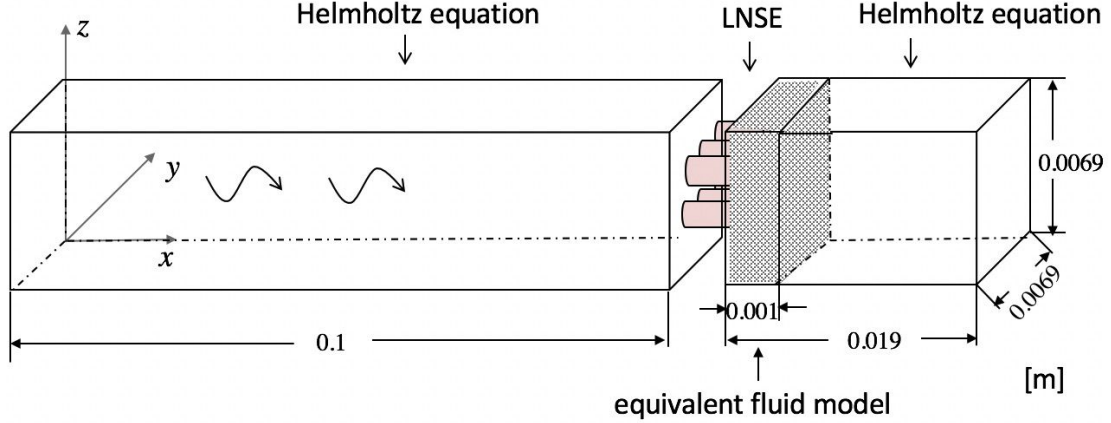


FIG. 5. The computational domain of the impedance duct installed with the hybrid liner. The acoustic methods constituting the ULNSE applied to the domain segments are outlined. The segment of the perforated plate with the use of the LNSE has a thickness of 1.2 mm.

by the small circular holes in the perforated plate) is imposed with the non-slip and rigid boundary condition:

$$\hat{u}_i = 0. \quad (33)$$

Moreover, all the walls in the computational domain are set with an additional isothermal boundary condition, pertaining to a constant temperature:

$$\hat{T} = 0. \quad (34)$$

C. Computational mesh

The simulation accuracy is affected by the mesh resolution in acoustic boundary layers. The thickness of an acoustic boundary layer is defined as:

$$\delta_A = \sqrt{\frac{2\mu}{\omega\rho_0}}, \quad (35)$$

This equation indicates that the acoustic boundary layer thickness is dependent on the angular frequency of a sound wave.

The current mesh generation strategy is demonstrated by testifying at the frequencies of 1000, 3000 and 5000 Hz. The generated meshes near the perforated plate holes are illustrated in Fig. 6. The frequencies result in the boundary layer thicknesses of $\delta_A = 6.96 \times 10^{-2}$, 4.02×10^{-2} and

3.11×10^{-2} mm in the perforated plate holes. As can be seen in the figure, the acoustic boundary layer becomes thin as the frequency increases.

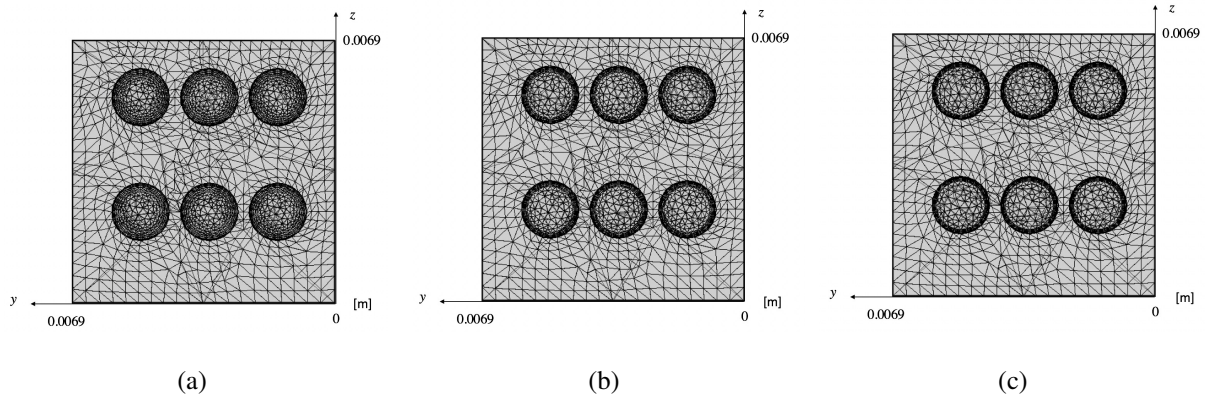


FIG. 6. The meshes with the refinement of the acoustic boundary layer in the perforated plate holes at the frequencies: (a) 1000 Hz, (b) 3000 Hz, and (c) 5000 Hz. The view from the incident acoustic wave direction.

The testified meshes for the sound waves at 1000, 3000 and 5000 Hz are adopted in the LNSE simulation of the corresponding waves. The acoustic particle velocity at 5000 Hz is shown in Fig. 7. As the results at the other frequencies are similar, they are not shown for the sake of brevity. The acoustic boundary layer is well resolved by the generated mesh. Thus, the present mesh generation strategy is sufficient for the following simulations involving the LNSE. The existence of the boundary layer proves the necessity of the use of the LNSE instead of the Helmholtz equation that is incapable of resolving boundary layers.

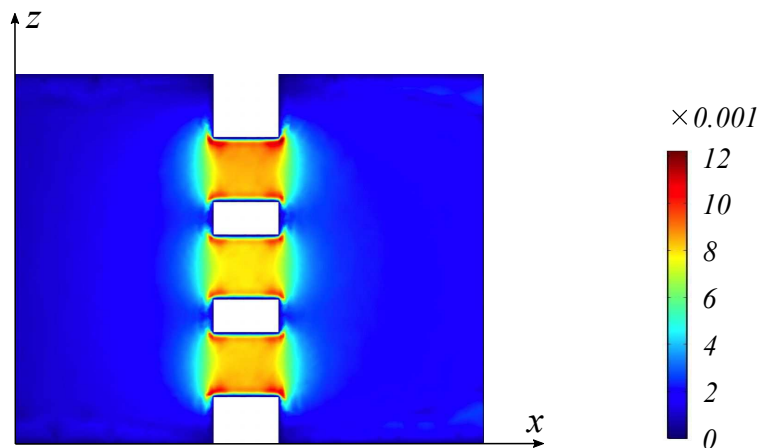


FIG. 7. Contours of the acoustic particle velocity near the perforated plate, to demonstrate the mesh generation strategy at the testified frequency of 5000 Hz. The unit of the acoustic particle velocity is $[m \cdot s^{-1}]$.

In the numerical modelling a sound source is applied at the upstream end of the impedance

duct. The excitation is in the plane wave regime from 1500 Hz to 5500 Hz yielding a maximum wavelength of the acoustic wave of 229 mm and a minimum wavelength of 63 mm. With a grid element size of 3 mm, there are at least 7 elements per wavelength for the highest numerical frequency⁴².

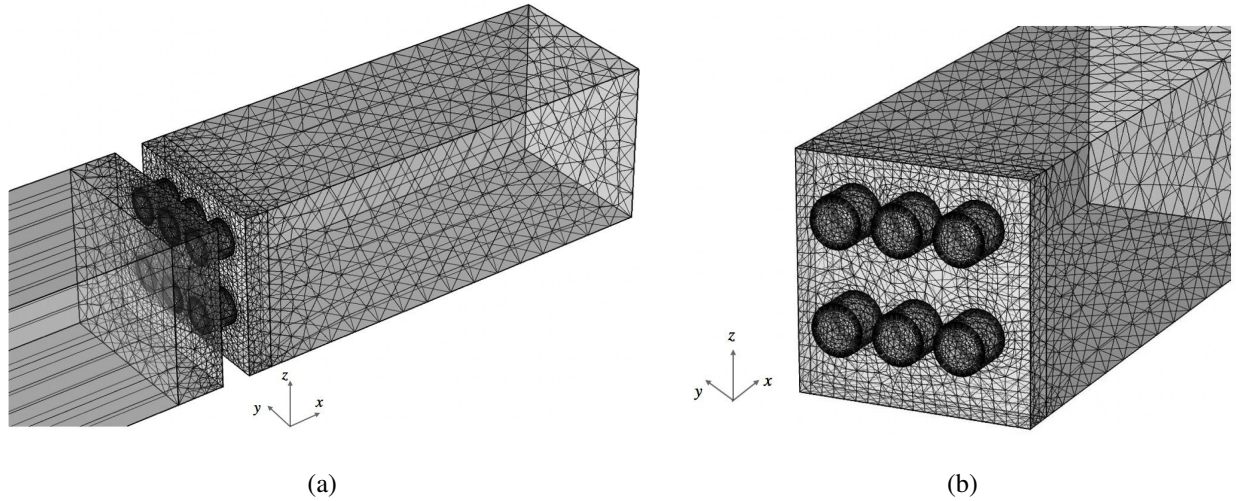


FIG. 8. (a) Overview of the mesh. (b) The mesh near the perforated plate.

The meshes used in the simulations are unstructured mesh with a total number of around 95 000 – 10000 elements, which varies with respect to the boundary layer thickness δ_A . An overview of the mesh and a closer view of the mesh at the perforated plate is shown in Fig. 8. The hybrid mesh consists of tetrahedrons in the cavity, a swept mesh in the straight duct and tetrahedrons in the boundary layer of the perforated plate. A transition zone with tetrahedrons is generated to connect the swept mesh and the tetrahedral mesh at the perforated plate. When the mesh is generated, a meshing technique for boundary layer adjustment is used, thus the thickness of the boundary layer is varying with the frequency. By using this technique, the mesh with the quality to resolve the acoustic boundary layer is generated.

D. Analysis of hybrid liner

1. Comparison of ULNSE and Helmholtz equation

Figure 9 shows isosurfaces of the acoustic pressure for a plane sound wave at 3000 Hz propagating within the duct and hybrid liner, which is computed using the ULNSE approach. The acoustic pressure decays along the propagation direction of the sound wave. Negative pressure is

found inside the hybrid liner and in the duct close to the perforated plate. Wave fronts are distorted to become relatively round near the perforated plate holes.

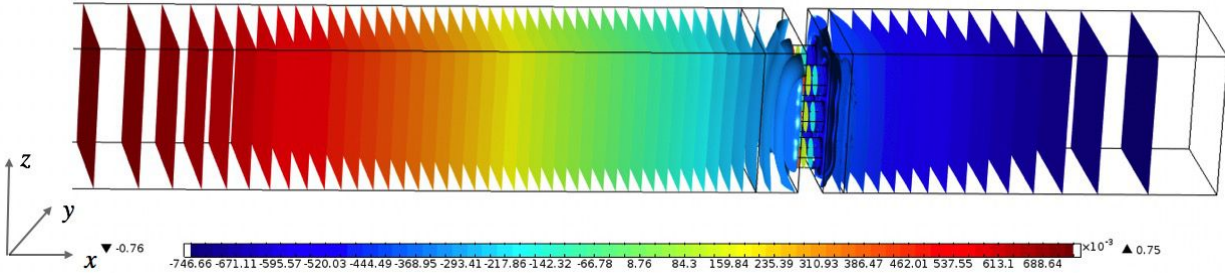


FIG. 9. Isosurfaces of the acoustic pressure (unit: Pa) generated by a sound wave at 3000 Hz.

In addition to the ULNSE, the hybrid liner is also simulated using the coupled original and modified Helmholtz equations. That is, the modified Helmholtz equation solving the equivalent fluid model is set for the domain segment of the metallic porous form, and the original Helmholtz equation is used in the rest of the computational domain including the perforated plate holes. The coupling algorithms imposed on the interfaces between the segments are the same as the ULNSE.

Figure 10 displays the acoustic characteristic coefficients of the hybrid liner that are computed using the ULNSE approach and the coupled original/modified Helmholtz equations. The parameters are the resistance and reactance of the acoustic impedance, and the magnitude and phase of the reflection coefficient. In comparison with the ULNSE, the coupled Helmholtz-equation approach shows obvious differences regarding the acoustic impedance resistance and the reflection coefficient magnitude. This suggests that the viscothermal losses inside the holes of the perforated plate play an important role in the sound propagation, as these effects can only be resolved by the ULNSE. The acoustic dissipation caused by the viscothermal losses introduces a significantly additional acoustic resistance into the hybrid liner system, and also reduces the reflection effect. On the other hand, the two approaches give similar predictions for the acoustic impedance reactance and reflection phase. It indicates that the viscothermal losses have limited influences on these acoustic characteristics.

2. *Effects of porous material*

To understand the effects of the foam that is placed next to the perforated plate, the foam is made of different porous materials such as glass fibre and mineral fibre in addition to the metal

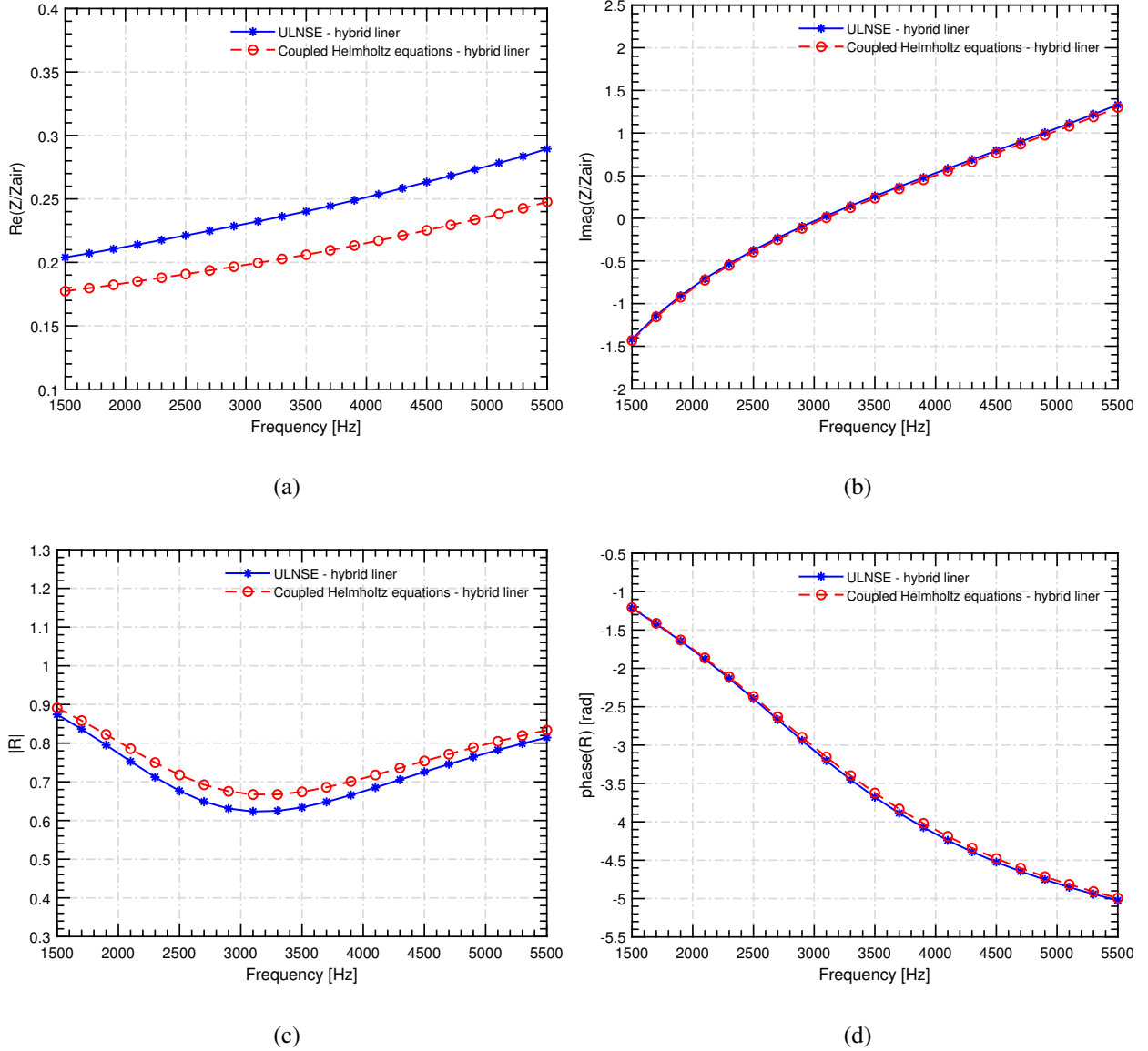


FIG. 10. The acoustic characteristic coefficients of the hybrid liner: (a) the resistance and (b) the reactance of the impedance, and (c) the magnitude and (d) the phase of the reflection coefficient. The numerical results of the ULNSE approach and the coupled original/modified Helmholtz equations are compared.

that is tested in the experiments - . The flow resistivity, σ , of the glass fibre (G1) is $4300 \text{ Pa} \cdot \text{s} \cdot \text{m}^{-2}$, and that of the mineral fibre (M2) is $15000 \text{ Pa} \cdot \text{s} \cdot \text{m}^{-2}$. The metallic foam has $34300 \text{ Pa} \cdot \text{s} \cdot \text{m}^{-2}$. As mentioned in the previous sections, the foam is modelled as an equivalent fluid within a porous medium. The modified Helmholtz equation is used to simulate this equivalent fluid.

The acoustic coefficients obtained from the different foam materials are shown in Fig. 11. The impedance resistance and reflection magnitude are obviously dependent on the flow resistivity. As

the flow resistivity becomes larger with the different porous materials, the impedance resistance of the hybrid liner is increased over all frequencies of interest between 1500 and 5500 Hz, while at the same time the reflection magnitudes are reduced. For all three materials, the troughs of the reflection magnitudes are seen between 3000 and 3500 Hz. Besides, the largest flow resistivity of the metallic foam leads to the most significant reduction in the reflection magnitudes within the magnitude trough zone, as compared with the other two materials. The impedance reactance and reflection phases are, however, almost not affected.

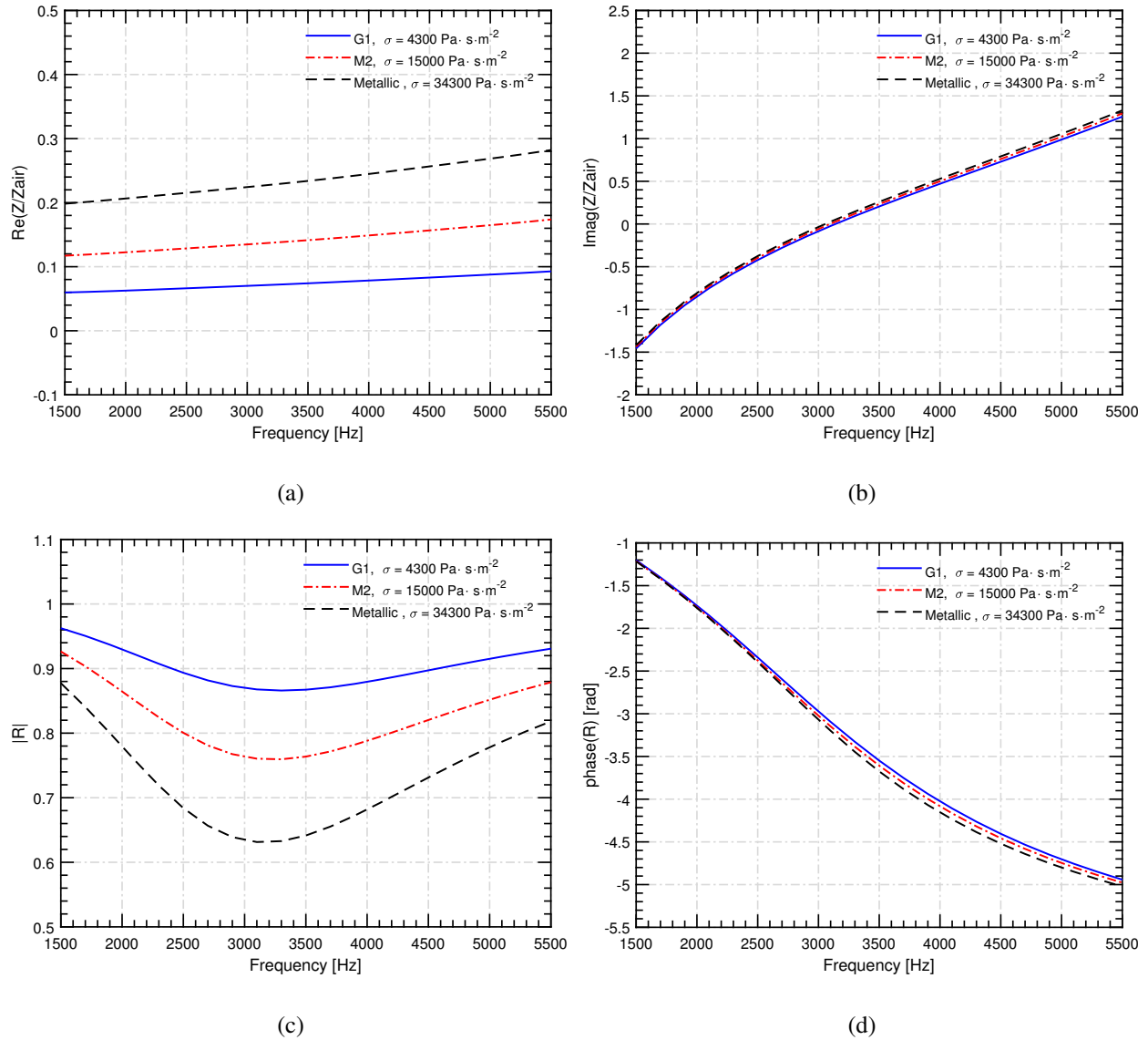


FIG. 11. The acoustic characteristic coefficients of the hybrid liner installed with the foams made of different materials: (a) the resistance and (b) the reactance of the impedance, and (c) the magnitude and (d) the phase of the reflection coefficient. The ULNSE approach is used.

V. APPLICATION OF ULNSE TO CONVENTIONAL LINERS

A. Conventional liners

The ULNSE approach is also applied to the simulation of conventional liners, which do not contain a porous foam next to the perforated plate. The geometry of a conventional liner and the setup for ULNSE are illustrated in Fig. 12. As compared with the numerical setup for the hybrid liner (see Fig. 5), the only different setting for the conventional liner is that there is no segment assigned with the equivalent fluid model since the porous foam is excluded. The critical geometric parameters of the perforated plates of the conventional liners (termed C-liners 1–3) are presented in Table I. The holes in the perforated plates have the same diameter of 1.5 mm. Given the plates of C-liners 1 and 2 contain 6 holes, the porosity is $\phi_p = 22.2\%$. And the set of 9 holes of C-liner 3 leads to $\phi_p = 33.3\%$. The thickness of the perforated plate is 1.2 mm for C-liners 1 and 3, and 0.6 mm for C-liner 2. These liners have been tested in experiments⁴³, and the test results are compared to the results of the current ULNSE and a semi-empirical model from a previous study⁴⁴ in the following analysis. The frequencies of interest range from 1500 Hz to 5500 Hz with an interval of 200 Hz.

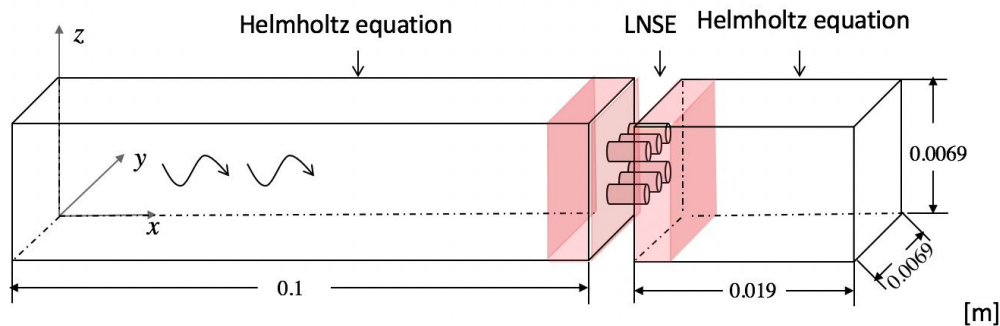


FIG. 12. The geometry of the conventional liner and the numerical setup of the ULNSE approach.

TABLE I. The geometric parameters of the perforated plates of the conventional liners⁴³.

Case No.	Perforation diameter (d)	Porosity (ϕ_p)	Plate thickness (t_p)
C-liner 1 (baseline)	1.5 [mm]	6 holes / 22.2%	1.2 [mm]
C-liner 2	1.5 [mm]	6 holes / 22.2%	0.6 [mm]
C-liner 3	1.5 [mm]	9 holes / 33.3%	1.2 [mm]

B. Semi-empirical model

A number of studies have been conducted to develop empirical or semi-empirical models for predicting the acoustic impedance of perforated plates with circular holes^{45–47}, although the mean flow is disregarded in the modeling. The present study adopts the semi-empirical model proposed by Bauer⁴⁴. The normalized acoustic impedance z_n of is modeled as:

$$z_n = \left[\left(\frac{\sqrt{8\mu\rho_0\omega}}{\rho_0 c_0 \phi_p} \right) \left(1 + \frac{t_p}{d} \right) \right] + i \left[\frac{k(t_p + 0.25d)}{\phi_p} - \cot(kH_c) \right], \quad (36)$$

where $\rho_0 c_0$ is the characteristic impedance of the fluid medium (i.e., air). The properties of the air are: the density $\rho_0 = 1.225 \text{ kg} \cdot \text{m}^{-3}$, the speed of sound $c_0 = 343 \text{ m} \cdot \text{s}^{-1}$, and the dynamic viscosity $\mu = 1.81 \times 10^{-5} \text{ kg} \cdot \text{m}^{-1} \cdot \text{s}^{-1}$. The perforated plate has the porosity ϕ_p and the thickness t_p . The diameter of circular holes is d . The depth of the cavity is $H_c = 0.019 \text{ m}$ in the present study.

The normalized acoustic impedance in Eq. 36 includes real and imaginary parts. The real part is the resistance of a liner that is dependent on the properties of the perforated plate. The imaginary part means the reactance caused by the perforated plate and cavity.

C. Effects of perforated plate thickness

As the perforated plate is the only component controlling sound wave propagation within a conventional liner, the critical parameters of the perforated plate can be explored based on the liners listed in Table I. To understand the effects of the plate thickness, C-liner 1 (the baseline case) and C-liner 2 are investigated, which have $t_p = 1.2$ and 0.6 mm , respectively. Both plates contain 6 holes with the same diameter of 1.5 mm .

Figure 13 shows the acoustic characteristic coefficients for C-liners 1 and 2. The results are obtained using the present ULNSE approach, Bauer's semi-empirical model⁴⁴, and from the previous experiments at KTH⁴³. The ULNSE results in general agree well with those of the semi-empirical model. On the other hand, the experimental results for the resistance and the reflection phase are different from ULNSE and semi-empirical modeling results, although the reactance and the reflection magnitudes from all three methods are similar. Compared to the experiments, the other two methods exhibit obvious discrepancies for the prediction of the resistance at relatively low frequencies. The reason is that the measured resistance has a decaying trend with respect to frequencies, but the results predicted with the other two methods increase with an approximately linear trend. Regarding the reflection magnitude, large discrepancies between the experiments and the other

two methods are mainly seen between 2500 and 4000 Hz. The discrepancies in the resistance and reflection magnitude might be caused by nonlinear effects or measurement uncertainties. The nonlinear effects are not considered in the simplified governing equations of the ULNSE approach, and are also missing in the semi-empirical model.

As can be seen in Fig. 13, as the thickness of the perforated plate increases from 0.6 mm to 1.2 mm, all three methods present similar trends in the evaluation of the acoustic characteristic coefficients, although the experimental results deviate from the other results as discussed above. The overall trends are: when the thickness increases, the resistance and reactance are enhanced, whereas the magnitude and phase of the reflection are reduced. Nevertheless, there are some exceptions such as the measured values of the resistance below 3000 Hz, the measured values of the reflection magnitude below 2000 Hz and above 3500 Hz, and the reflection magnitude obtained using the ULNSE and semi-empirical model at comparatively high frequencies larger than 4700 Hz.

D. Effects of perforated plate porosity

The porosity effects of the perforated plate on the acoustic performance are analyzed by comparing C-liners 1 and 3 (see Table I. The difference between the two liner geometries is that the perforated plate of C-liner 1 has 6 holes, whereas that of C-liner 3 has 9 holes. Consequently, the plate porosity is 22.2% for C-liner 1 and 33.3% for C-liner-3.

The acoustic impedance and reflection coefficients of these liners are displayed in Fig. 14. The experimental results show larger differences in the resistance and reflection magnitude, compared to the ULNSE and semi-empirical approaches. This phenomenon is also observed in Fig. 13, which could be attributed to the neglect of nonlinear effects in the numerical and modeling methods. Despite this, the three methods provide similar trends in capturing the reactance and reflection coefficients.

As can be seen in Fig 14, increasing the porosity gives rise to reduced resistance and reactance of the acoustic impedance, but the reflection magnitude and phase are increased correspondingly. These effects are generally identified using all three methods, despite a small inconsistency existing in the measured reflection magnitude at the frequencies above 4300 Hz. By cross-comparing Figs. 13 and 14, it is found that the impedance coefficients are always changed oppositely against the reflection coefficients When the liner geometric parameters are adjusted.

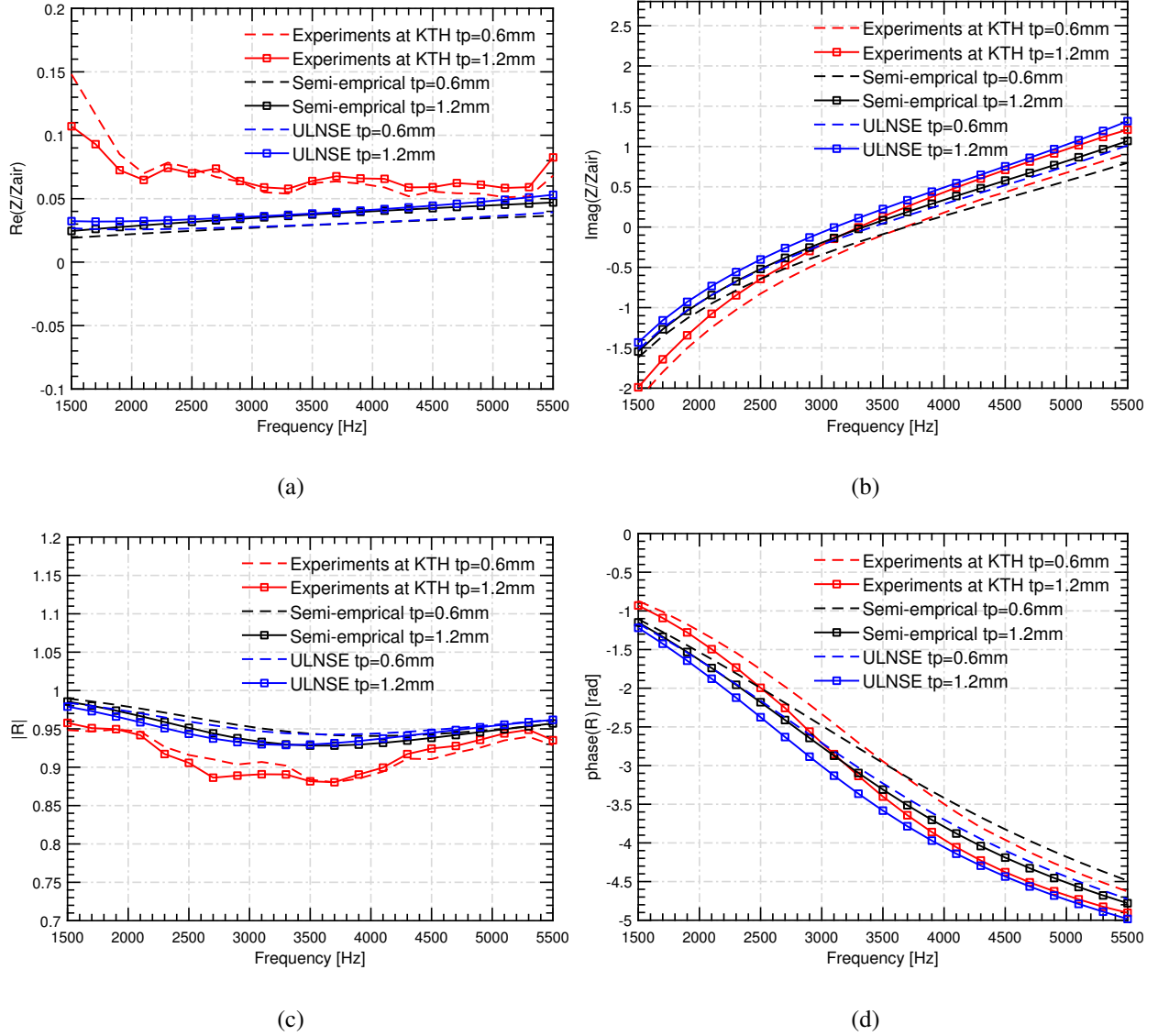


FIG. 13. The acoustic characteristic coefficients of the conventional liners (C-liners 1 and 2) with the perforated plate thickness of $t_p = 1.2$ and 0.6 , respectively. (a) The resistance and (b) the reactance of the impedance. (c) The magnitude and (d) the phase of the reflection coefficient.

VI. DISCUSSION OF HYBRID AND CONVENTIONAL LINERS

The hybrid liner is installed an additional porous metallic foam compare to the conventional baseline liner, C-liner 1 (see Table I). The foam has a thickness of $t_f = 1$ mm and the flow resistivity $[\sigma] = 34300 \text{ Pa} \cdot \text{s} \cdot \text{m}^{-2}$.

Figure 15 shows the impedance and reflection coefficients of the hybrid liner and C-liner 1, which are measured in the experiments at KTH MWL⁴³ and computed using the current ULNSE

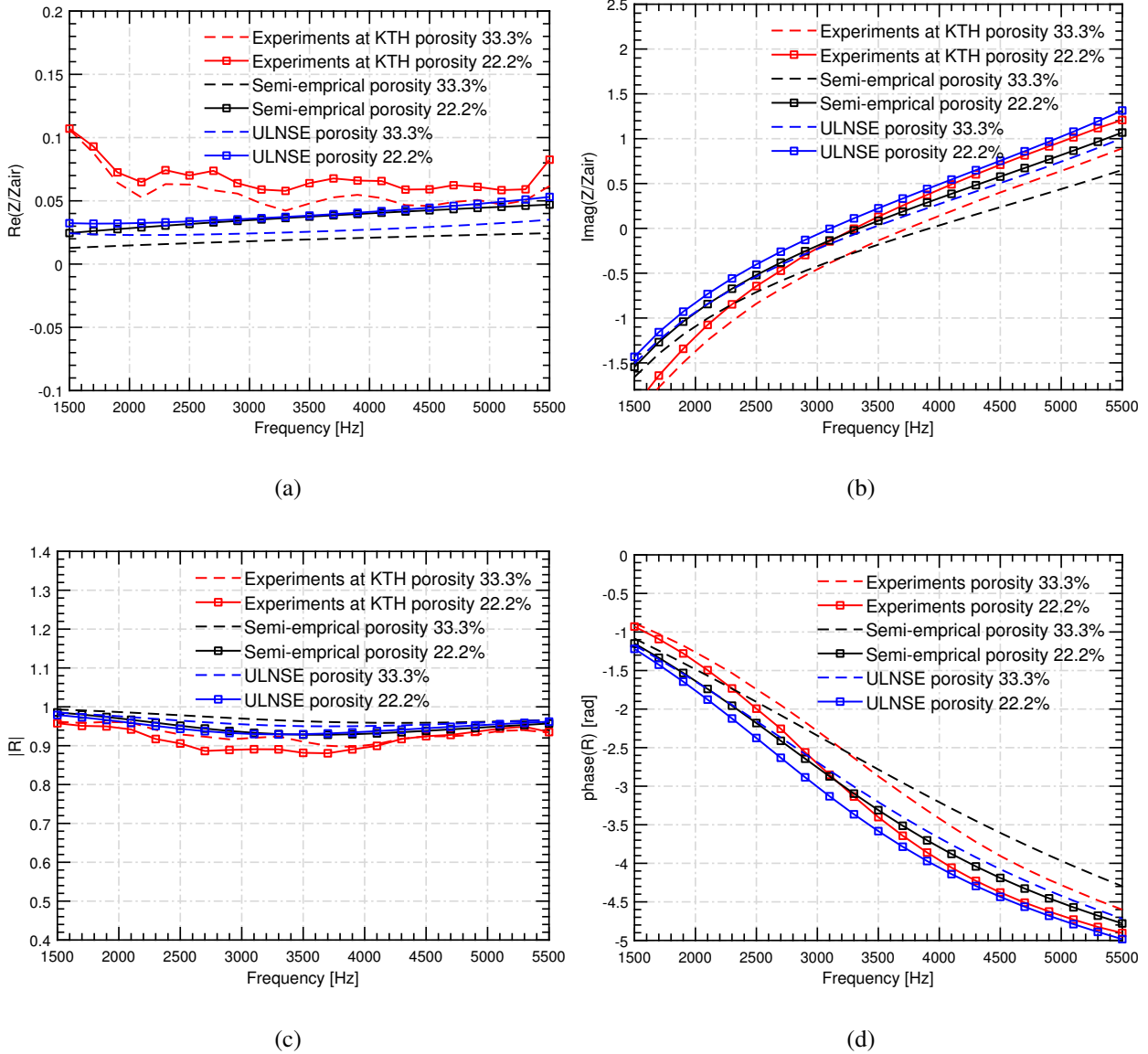


FIG. 14. The acoustic characteristic coefficients of the conventional liners, C-liners 1 and 3, with the perforated plate porosity of $\phi_p = 22.2\%$ (6 holes contained in the perforated plate) and 33.3% (9 holes), respectively. The acoustic impedance coefficients: (a) the resistance and (b) the reactance. The reflection coefficients: (c) the magnitude and (d) the phase.

method. The numerical results are in overall agreement with the experimental results. Nevertheless, obvious differences between the numerical and experimental results are seen for the resistance and the reflection magnitude of C-liner 1. A possible reason for low frequency deviations in normalized resistance and reflection magnitude could be that there are very small leakages between the assembled test samples and the tube wall. Regarding the reactance and the reflection phase, the differences mainly exist at frequencies below 3500 Hz. It is interesting to see that the ULNSE

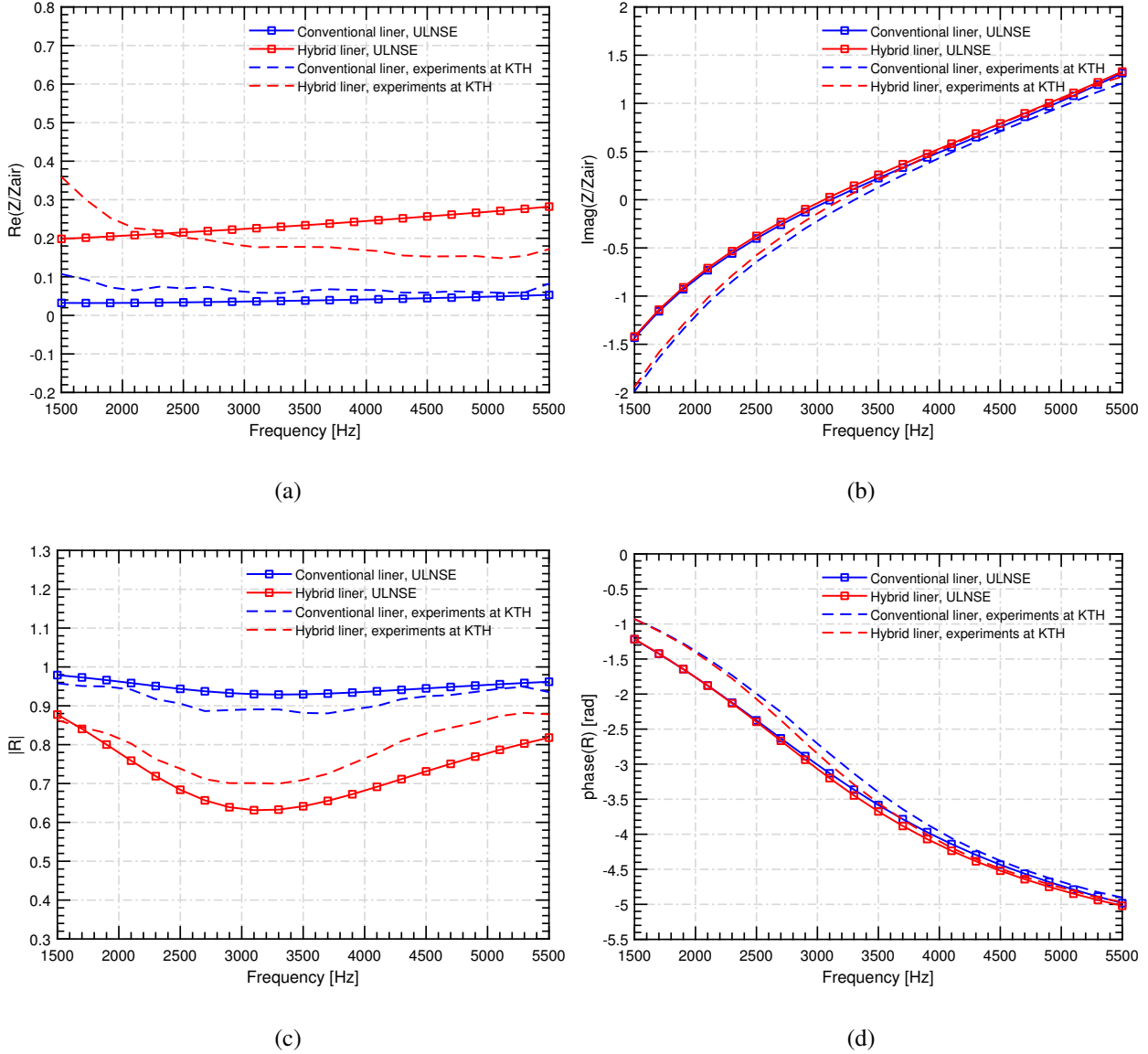


FIG. 15. Comparison of the hybrid liner and the baseline conventional liner – C-liner 1. The acoustic impedance coefficients: (a) the resistance and (b) the reactance. The reflection coefficients: (c) the magnitude and (d) the phase.

overestimates the resistance of the hybrid liner above 2200 Hz but underestimates this variable for C-liner 1 at all frequencies of interest. Conversely, the reflection magnitude predicted with the ULNSE is underestimated for the hybrid liner but overestimated for C-liner 1. The results of the hybrid liner exhibit the largest differences in the resistance and reflection magnitudes between the methods. The measurement uncertainties for the resistivity of the metallic foam could account for the discrepancies. Moreover, since the thickness of the porous metallic foam is only 1 mm, elastic

deformations of the structure can be stimulated by sound waves during the tests. But this effect is not considered in the present ULNSE method.

Comparing the hybrid liner and C-liner 1 in Fig. 15, a common observation is that the metallic foam brings about small changes into the reactance and the reflection phase. This is observed in both numerical and experimental results. However, the resistance and the reflection magnitude are significantly altered owing to the metallic foam. According to the ULNSE results, the resistance of C-liner 1 is around 0.05, while that of the hybrid liner is increased to the range from 0.2 to 0.3 because of the inclusion of the metallic foam. The experimental results present in a similar trend: the metallic foam increases the resistance of 0.05 – 0.1 for C-liner 1 to 0.15 – 0.35 for the hybrid liner. In contrast, the reflection magnitude is noticeably reduced by the metallic foam. The ULNSE approach produces the prediction that this coefficient of C-liner 1 is 0.87 at 1500 Hz, and decays to 0.61 at nearly 3200 Hz. It then rises to 0.81 at 5500 Hz. Although a trough of this coefficient predicted with ULNSE is also observed for the hybrid liner, it is much smaller. Its maximum value is 0.98 at 1500 Hz, and the minimum value is 0.93 at about 3250 Hz. Despite that there are discrepancies between the numerical and experimental results, it is seen that the reflection magnitude measured also shows a similar trend.

VII. CONCLUSIONS

A unified linearized Navier-Stocks equations (ULNSE) approach in the frequency domain is proposed for 3D scenarios in the present study. This approach couples the classical LNSE, the original form of the Helmholtz equation, and a modified form of the Helmholtz equation that takes into account an equivalent fluid model for porous mediums. The coupling algorithms of the ULNSE approach are put forward and validated. The proposed approach is numerically implemented based on the finite element method. In principle, it can also be used for other numerical methods, for example finite volume methods. The ULNSE approach enables separate definitions and settings for different regions, given that the acoustic wave propagation is dependent on local fluid and structure conditions. In particular, local viscothermal effects can be resolved using the classical LNSE, and the acoustic wave propagation in porous mediums can be modelled by the modified Helmholtz equation. If only plane waves propagate, the Helmholtz equation is sufficient for the simulation, and its computational costs are much more lower than the classical LNSE. Thus, the advantage of the ULNSE approach is that it uses much less computational resources but

maintains numerical accuracy in comparison with the classical LNSE.

The ULNSE approach is validated and applied to simulate a hybrid acoustic liner in which a porous foam is assembled next to a perforated plate, i.e., the outlet of the liner cavity connecting to an external duct. The porous foam is the only difference between the hybrid liner and conventional liners, which are also investigated in this study. Moreover, it is necessary to use the LNSE in the simulation of the acoustic wave propagation in the porous foam, since the foam accounts for viscothermal losses. The simulation results of a set of hybrid and conventional liners using the approach are compared to those from Bauer's semi-empirical model⁴⁴ and from the experiments⁴³.

Three materials (glass fibre, mineral fibre, and metal) are used to make porous foams for the hybrid liner. Correspondingly, the flow resistivity is increased in the order. The flow resistivity is found having a significant effect on the impedance resistance and reflection magnitude, while its influence on the impedance reactance and reflection phase is nearly negligible. Increasing the flow resistivity results in an increase in the impedance resistance but a reduction in the reflection magnitude over the frequency band of interest (1500 – 5500 Hz). Furthermore, a comparison of the hybrid liner and the baseline conventional liner also proves that the metallic porous foam has a very minor effect on the impedance reactance and reflection phase. On the other hand, the porous foam significantly increases the impedance resistance but reduces reflection magnitude. This means that the hybrid liner mounted with the porous foam has better acoustic performance than the conventional liner without the porous foam.

The perforated plate between the liner cavity and external duct is analyzed in terms of its thickness and porosity. The porosity is derived based on the number of holes in the perforated plate. The porosity of 6 and 9 holes is 22.2% and 33.3%, respectively. As the plate thickness increases, the resistance and reactance of the impedance are enhanced. Conversely, the magnitude and phase of the reflection are decreased. Regarding the porosity, an increase in this parameter causes reduced resistance and reactance, but increased reflection magnitude and phase.

The present ULNSE approach can be extended to consider a moving medium where the flow has a convection effect on the sound wave propagation. This is realized by an additional convection term that is included in the governing equations of the present approach²⁰. In addition to aerospace applications, similar scenarios of noise in ducts are also noticed in other fields, for example, fans in HVAC systems^{48,49}. It will be interesting to apply the current technology of liners to noise absorption in such scenarios.

ACKNOWLEDGMENTS

The presented work is part of the Marie Curie Initial Training Network Thermo-acoustic and aero-acoustic nonlinearities in green combustors with orifice structures (TANGO). We gratefully acknowledge the financial support from the European Commission under the call FP7-PEOPLE-ITN-2012. The simulations were performed at the facilities within the PDC centre for high performance computing at KTH in Stockholm.

REFERENCES

- ¹W. Neise and L. Enghardt, “Technology approach to aero engine noise reduction,” *Aerospace Science and Technology* **7**, 352–363 (2003), [http://dx.doi.org/10.1016/S1270-9638\(03\)00027-0](http://dx.doi.org/10.1016/S1270-9638(03)00027-0).
- ²Z. Huang, H.-D. Yao, O. Sjögren, A. Lundbladh, and L. Davidson, “Aeroacoustic analysis of aerodynamically optimized joined-blade propeller for future electric aircraft at cruise and take-off,” *Aerospace Science and Technology* **107**, 106336 (2020), <https://doi.org/10.1016/j.ast.2020.106336>.
- ³E. Envia, “Fan noise reduction: an overview,” *International Journal of Aeroacoustics* **1**, 43–64 (2002), <https://doi.org/10.1260/1475472021502668>.
- ⁴H. Yao, L. Davidson, S.-H. Peng, M. B. Francesco Capizzano, and G. Mingione, “Assessment of conceptual noise reduction devices for a main landing gear using sngr method,” in *21st AIAA/CEAS Aeroacoustics Conference* (Dallas, Texas, 2015) pp. 2015–2692, <https://doi.org/10.2514/6.2015-2692>.
- ⁵C. K. Tam, H. Ju, M. G. Jones, W. R. Watson, and T. L. Parrott, “A computational and experimental study of resonators in three dimensions,” *Journal of Sound and Vibration* **329**, 5164–5193 (2010), <https://doi.org/10.1016/j.jsv.2010.06.005>.
- ⁶L. Zhou and H. Bodén, “A systematic uncertainty analysis for liner impedance reduction technology,” *Journal of Sound and Vibration* **356**, 86–99 (2015), <https://doi.org/10.1016/j.jsv.2015.07.001>.
- ⁷R. Kabral, L. Du, and M. Åbom, “Optimum sound attenuation in flow ducts based on the “exact” cremer impedance,” *Acta Acustica United with Acustica* **102**, 851–860 (2016), <https://doi.org/10.3813/AAA.918999>.

- ⁸J. Gikadi, S. Föller, and T. Sattelmayer, “Impact of turbulence on the prediction of linear aeroacoustic interactions: Acoustic response of a turbulent shear layer,” *Journal of Sound and Vibration* **333**, 6548–6559 (2014), <https://doi.org/10.1016/j.jsv.2014.06.033>.
- ⁹M. A. Temiz, I. L. Arteaga, G. Efraimsson, M. Åbom, and A. Hirschberg, “The influence of edge geometry on end-correction coefficients in micro perforated plates,” *The Journal of the Acoustical Society of America* **138**, 3668–3677 (2015), <https://doi.org/10.1121/1.4937748>.
- ¹⁰J. Tournadre, K. Förner, W. Polifke, P. Martínez-Lera, and W. Desmet, “Determination of acoustic impedance for Helmholtz resonators through incompressible unsteady flow simulations,” *AIAA Journal* **55**, 1–9 (2016), <https://doi.org/10.2514/1.J055337>.
- ¹¹E. Alenius, M. Åbom, and L. Fuchs, “Large eddy simulations of acoustic-flow interaction at an orifice plate,” *Journal of Sound and Vibration* **345**, 162–177 (2015), <https://doi.org/10.1016/j.jsv.2015.02.012>.
- ¹²S. Sack and M. Åbom, “Investigation of orifice aeroacoustics by means of multi-port methods,” *Journal of Sound and Vibration* **407**, 32–45 (2017), <https://doi.org/10.1016/j.jsv.2017.06.026>.
- ¹³Q. Zhang and D. J. Bodony, “Numerical investigation of a honeycomb liner grazed by laminar and turbulent boundary layers,” *Journal of Fluid Mechanics* **792**, 936–980 (2016), <https://doi.org/10.1017/jfm.2016.79>.
- ¹⁴C. Sovardi, S. Jaensch, and W. Polifke, “Concurrent identification of aero-acoustic scattering and noise sources at a flow duct singularity in low Mach number flow,” *Journal of Sound and Vibration* **377**, 90–105 (2016), <https://doi.org/10.1016/j.jsv.2016.05.025>.
- ¹⁵H.-D. Yao and L. Davidson, “Vibro-acoustics response of a simplified glass window excited by the turbulent wake of a quarter-spherocylinder body,” *The Journal of the Acoustical Society of America* **145**, 3163 (2019), <https://doi.org/10.1121/1.51095482>.
- ¹⁶Y. Aurégan, R. Starobinski, and V. Pagneux, “Influence of grazing flow and dissipation effects on the acoustic boundary conditions at a lined wall,” *The Journal of the Acoustical Society of America* **109**, 59–64 (2001), <https://doi.org/10.1121/1.1331678>.
- ¹⁷C. Weng, S. Boij, and A. Hanifi, “On the calculation of the complex wavenumber of plane waves in rigid-walled low-mach-number turbulent pipe flows,” *Journal of Sound and Vibration* **354**, 132–153 (2015), <https://doi.org/10.1016/j.jsv.2015.06.013>.
- ¹⁸D. Khamis and E. J. Brambley, “Viscous effects on the acoustics and stability of a shear layer

- over an impedance wall,” *Journal of Fluid Mechanics* **810**, 489–534 (2017), <https://doi.org/10.1017/jfm.2016.737>.
- ¹⁹F. Caeiro, C. Sovardi, K. a. Förner, and W. Polifke, “Shape optimization of a Helmholtz resonator using an adjoint method,” *International Journal of Spray and Combustion Dynamics* **9**, 394–408 (2017), <https://doi.org/10.1177/1756827717703576>.
- ²⁰S. Vandemaele, H. Denayer, W. De Roeck, and W. Desmet, “Numerical modeling of the flow acoustic behavior of sub-millimeter orifices in 3D using linearized Navier-Stokes equations,” in *25th AIAA/CEAS Aeroacoustics Conference* (2019) p. 2628, <https://doi.org/10.2514/6.2019-2628>.
- ²¹A. Kierkegaard, S. Boij, and G. Efrimsson, “A frequency domain linearized Navier-Stokes equations approach to acoustic propagation in flow ducts with sharp edges,” *The Journal of the Acoustical Society of America* **127**, 710–719 (2010), <https://doi.org/10.1121/1.3273899>.
- ²²A. Kierkegaard, S. Allam, G. Efrimsson, and M. Åbom, “Simulations of whistling and the whistling potentiality of an in-duct orifice with linear aeroacoustics,” *Journal of Sound and Vibration* **331**, 1084–1096 (2012), <https://doi.org/10.1016/j.jsv.2011.10.028>.
- ²³A. Kierkegaard, S. Boij, and G. Efrimsson, “Simulations of the scattering of sound waves at a sudden area expansion,” *Journal of Sound and Vibration* **331**, 1068–1083 (2012), <https://doi.org/10.1016/j.jsv.2011.09.011>.
- ²⁴A. Holmberg, A. Kierkegaard, and C. Weng, “A frequency domain linearized Navier-Stokes method including acoustic damping by eddy viscosity using Rans,” *Journal of Sound and Vibration* **346**, 229–247 (2015), <https://doi.org/10.1016/j.jsv.2015.02.030>.
- ²⁵C. Weng, S. Boij, and A. Hanifi, “On the calculation of the complex wavenumber of plane waves in rigid-walled low-mach-number turbulent pipe flows,” *Journal of Sound and Vibration* **354**, 132 – 153 (2015).
- ²⁶S. Sack, M. Abom, and G. Efrimsson, “On acoustic multi-port characterisation including higher order modes,” *Acta Acustica United with Acustica* **102**, 834–850 (2016), <https://doi.org/10.1016/j.jsv.2017.06.026>.
- ²⁷A. Kierkegaard, G. Efrimsson, and A. Agarwal, “Linear simulations of liners sandwiched with a metal foam,” in *19th AIAA/CEAS Aeroacoustics Conference* (2013) <https://doi.org/10.2514/6.2013-2272>.
- ²⁸W. Na, G. Efrimsson, and S.Boij, “,” in *ICSV 21: The 21st International Congress on Sound*

- and Vibration* (2014).
- ²⁹A. D. Pierce, *Acoustics: An Introduction to Its Physical Principles and Applications* (The Acoustical Society of America, 1991).
- ³⁰F. M. White and I. Corfield, , Vol. 3 (McGraw-Hill, New York, 2006).
- ³¹C. Weng, *Theoretical and numerical studies of sound propagation in low-Mach-number duct flows*, Ph.D. thesis, KTH Royal Institute of Technology (2015).
- ³²S. W. Rienstra and A. Hirschberg, “An Introduction to Acoustics,” *Eindhoven University of Technology* **18**, 19 (2003).
- ³³J. D. Anderson and J. Wendt, , Vol. 206 (Springer, 1995).
- ³⁴W. Na, *A Linearized Navier-Stokes Equations Methodology for Aeroacoustic and Thermoacoustic Simulations*, Ph.D. thesis, KTH Royal Institute of Technology (2021).
- ³⁵J. Allard and N. Atalla, *Propagation of Sound in Porous Media: Modelling Sound Absorbing Materials* (John Wiley & Sons, 2009).
- ³⁶Y. Miki, “Acoustical properties of porous materials. modifications of Delany-Bazley models.” *Journal of the Acoustical Society of Japan (E)* **11**, 19–24 (1990), <https://doi.org/10.1250/ast.11.19>.
- ³⁷T. J. Hughes, *The Finite Element Method: Linear Static and Dynamic Finite Element Analysis* (Courier Corporation, 2012).
- ³⁸J. Donea and A. Huerta, *Finite element methods for flow problems* (John Wiley & Sons, 2003) <https://doi.org/10.1002/0470013826>.
- ³⁹H. Bodén and M. Åbom, “Influence of errors on the two-microphone method for measuring acoustic properties in ducts,” *The Journal of the Acoustical Society of America* **79**, 541–549 (1986), <https://doi.org/10.1121/1.393542>.
- ⁴⁰M. Åbom and H. Bodén, “Error analysis of two-microphone measurements in ducts with flow,” *The Journal of the Acoustical Society of America* **83**, 2429–2438 (1988), <https://doi.org/10.1121/1.396322>.
- ⁴¹S. Allam and M. Åbom, “Investigation of damping and radiation using full plane wave decomposition in ducts,” *Journal of Sound and Vibration* **292**, 519–534 (2006), <https://doi.org/10.1016/j.jsv.2005.08.016>.
- ⁴²S. Marburg, “Discretization requirements: How many elements per wavelength are necessary?” in *Computational Acoustics of Noise Propagation in Fluids-Finite and Boundary Element Methods* (Springer, 2008).

- ⁴³R. Kabral, H. Bodén, and T. Elnady, “Determination of liner impedance under high temperature and grazing flow conditions,” in *20th AIAA/CEAS Aeroacoustics Conference* (2014) <https://doi.org/10.2514/6.2014-2956>.
- ⁴⁴A. B. Bauer, “Impedance theory and measurements on porous acoustic liners,” *Journal of Aircraft* **14**, 720–728 (1977), <https://doi.org/10.2514/3.58844>.
- ⁴⁵S.-H. Lee and J.-G. Ih, “Empirical model of the acoustic impedance of a circular orifice in grazing mean flow,” *The Journal of the Acoustical Society of America* **114**, 98–113 (2003), <https://doi.org/10.1121/1.1581280>.
- ⁴⁶J. W. Sullivan, “A method for modeling perforated tube muffler components. II. Applications,” *The Journal of the Acoustical Society of America* **66**, 779–788 (1979), <https://doi.org/10.1121/1.383680>.
- ⁴⁷A. Hersh, B. Walker, and J. Celano, “Helmholtz resonator impedance model, part 1: Nonlinear behavior,” *AIAA journal* **41**, 795–808 (2003), <https://doi.org/10.2514/2.2041>.
- ⁴⁸M. Ottersten, H.-D. Yao, and L. Davidson, “Inlet gap effect on aerodynamics and tonal noise generation of a voluteless centrifugal fan,” *Physics of Fluids* **33**, 075110 (2021), <https://doi.org/10.1063/5.0055242>.
- ⁴⁹M. Ottersten, H.-D. Yao, and L. Davidson, “Inlet gap effect on aerodynamics and tonal noise generation of a voluteless centrifugal fan,” *Journal of Sound and Vibration* **540**, 117304 (2022), <https://doi.org/10.1016/j.jsv.2022.117304>.